Asymmetry in shape causing absolute negative mobility

Peter Hänggi,[1] Fabio Marchesoni,[2] Sergey Savel'ev,[3] and Gerhard Schmid[1]

[1]*Institut für Physik, Universität Augsburg, D-86159 Augsburg, Germany*
[2]*Dipartimento di Fisica, Università di Camerino, I-62032 Camerino, Italy*
[3]*Department of Physics, Loughborough University, Loughborough LE11 3TU, United Kingdom*

We propose a simple classical concept of nanodevices working in an absolute negative mobility (ANM) regime: the minimal spatial asymmetry required for ANM to occur is embedded in the geometry of the transported particle, rather than in the channel design. This allows for a tremendous simplification of device engineering, thus paving the way toward practical implementations of ANM. Operating conditions and performance of our model device are investigated, both numerically and analytically.

I. INTRODUCTION

Realizing a micro- or nanodevice exhibiting *absolute negative mobility* (ANM) poses serious technological challenges, as this task is believed to require finely tailored spatial asymmetries either in the (nonlinear) particle-particle interactions [1,2] or, more conveniently, in the geometry of the device itself [3,4]. A device is said to operate in the ANM regime, when it works steadily against a biased force, i.e., a force with nonzero stationary mean. According to the Second Law of Thermodynamics (or more precisely, the so called principle of Le Chatelier), a static force alone cannot induce ANM in a device coupled to an equilibrium heat bath, unless an additional time dependent force is applied to bring the system out of equilibrium. ANM is known to occur as a genuine *quantum mechanical* phenomenon in photovoltaic materials, as the result of photoassisted tunneling in either the bulk of noncentrosymmetric crystals [5] or artificial semiconductor structures [6,7]. However, such manifestations of the ANM phenomenon do not survive in the limit of a classical description, so that detecting ANM in a purely classical system remains a challenging task.

As spatial symmetry typically suppresses ANM, *ad hoc* contrived geometries have been proposed to circumvent this difficulty. The most promising solution devised to date, is represented by two-dimensional (2D) or three-dimensional (3D) channels with inner walls tailored so as to force the transported particles along meandering paths [3,4], a design that can be implemented, e.g., in superconducting vortex devices [8]. Other classical set-ups advocate elusive dynamic chaotic effects [9–11]. Although such finely tuned asymmetric geometries and/or nonlinear dynamic behaviors may seem hardly accessible to table-top experiments, first convincing demonstrations of classical ANM have actually been obtained following this strategy [12,13].

We propose here a much simpler, affordable working concept for a classical ANM device, by embedding the spatial asymmetry into the shape of the transported particles, rather than in the channel geometry. In view of this new formulation, the ANM mechanism is expected to occur in natural systems, too, where cylindrically symmetric channels in low spatial dimensions and elongated particles are frequently encountered [14,15].

This paper is organized as follows. We introduce in Sec. II the Langevin equations for a floating ellipsoidal Brownian particle ac-driven along a 2D compartmentalized channel. By numerical simulation we show in Sec. III that ANM actually occurs as an effect of the particle elongation. In Sec. IV, we analyze the dependence of ANM on both the drive parameters and the particle geometry, with the purpose of determining the optimal operating conditions of our model device. Finally, in Sec. V, we discuss the applicability of the proposed ANM mechanism to nanoparticle transport in realistic biological and artificial devices.

II. MODEL

Let us consider an elongated Brownian particle, shaped as an elliptic disk, moving in a straight 2D channel (Fig. 1). The overdamped dynamics of the particle is modeled by three Langevin equations, namely,

$$\frac{d\vec{r}}{dt} = -F(t)\vec{e}_x + \sqrt{D_r}\vec{\xi}(t); \tag{1a}$$

$$\frac{d\phi}{dt} = \sqrt{D_\phi}\xi_\phi(t), \tag{1b}$$

where $\vec{e}_x, \vec{e}_y$ are the unit vectors along the x, y axes, $\vec{r} \equiv (x, y)$ denotes the particle center of mass, and ϕ is the
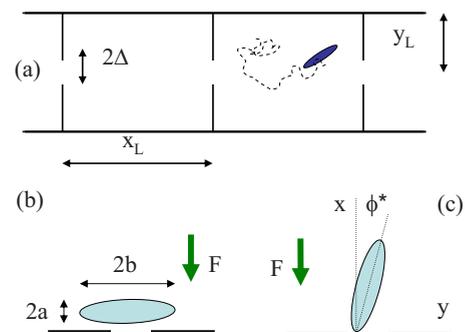
FIG. 1. (Color online) (a) Asymmetric particle tumbling in a periodically segmented 2D channel. The pores, 2Δ wide, are centered on the channel axis. (b) Elliptic particle with semiaxes a and b, at rest against a compartment wall. Note that $a < \Delta < b$. (c) Elliptic particle in escape position, its major axis forming a maximum angle ϕ^* with the channel axis.

orientation of its major axis with respect to the channel axis, $\vec{e}_x$. Here, $\vec{\xi}(t) \equiv [\xi_x(t), \xi_y(t)]$ and $\xi_\phi(t)$ are zero-mean, white Gaussian noises with autocorrelation functions $\langle \xi_i(t) \xi_j(t') \rangle = 2\delta_{ij}\delta(t-t')$ and $i,j = x,y,\phi$. The channel is periodically segmented by means of orthogonal compartment walls, each bearing an opening, or pore, of half-width Δ, placed at its center [16]. As sketched in Fig. 1(a), the channel is mirror symmetric with respect to both its longitudinal axis and each compartment wall. This is an important difference with Refs. [3,4], where the channel confining potential, $V(x,y)$, was taken to be asymmetric under both mirror reflections—although symmetric under double reflection, $V(-x,y) \doteq V(x,-y)$.

In order to detect ANM, the particle must be driven in a pulsating manner parallel to the channel axis. This means that $F(t)$ consists of at least two terms [3,4]: a dc drive, F_0, and an unbiased, symmetric ac drive, $F_{ac}(t)$, with amplitude $\max\{|F_{ac}(t)|\} = F_1$ and temporal period T_Ω. Accordingly, the waveform of $F_{ac}(t)$ is subjected to the conditions $\langle F_{ac}^{(2n+1)}(t) \rangle_\Omega = 0$, with $n = 0,1,2\ldots$ and $\langle \ldots \rangle_\Omega$ denoting the time average taken over one drive cycle [17].

Equations (1) have been numerically integrated for an elliptic disk of semiaxes a and b, under the assumption that the channel walls were perfectly reflecting and the particle-wall collisions were elastic [18]. In the following we report the outcome of extensive simulations for a fixed channel compartment geometry, $x_L = y_L$, $\Delta/y_L \ll 1$, but different particle elongations, b/a, ac-drive waveforms, and ratios of the rotational to translational diffusion coefficients, D_ϕ/D_r. We conclude that ANM occurs in such a highly symmetric channel geometry only because of the elongated aspect ratio of the drifting particle.

As illustrated in panels (b) and (c) of Fig. 1, an elliptic disk with $a < \Delta < b$ crosses a narrow pore only when its major semiaxis forms a small angle with the channel axis, $|\phi| \leq \phi^*$. For $a \ll b$ (rodlike particle) as in most of our simulations, $\sin \phi^* \simeq \Delta/b$. To overcome the escape angle ϕ^* from a rest position with $\phi = \pi/2$, the disk must rotate against the total applied force, $F(t) = F_0 + F_{ac}(t)$. For $F_0 < F_1$ this is more easily achieved for pore crossings occurring in the direction of $F_{ac}(t)$, but opposite to the static force F_0. As a result, under appropriate conditions, detailed below, the net particle current, $\langle v \rangle$, may indeed flow in the direction *opposite* to F_0.

III. ANM MECHANISM

In order to explain the appearance of ANM, we start looking at the mobility of an elongated particle driven by a constant force F (Fig. 2, inset). Let $v(F)$ denote its steady velocity and $\mu(F) = v(F)/F$ the relevant mobility, with $\mu(-F) = \mu(F)$. From now on, and until stated otherwise, we set for simplicity $D_r = D_\phi = D$, so that μ is a function of F/D. At equilibrium with $F = 0$, $\mu_0 \equiv \mu(0)$ is a D-independent constant, which strongly depends on both the compartment and the particle geometry as discussed below. For zero drive, the particle rotates away from the walls; pore crossing is thus controlled mostly by *translational* diffusion.

As the magnitude of the applied force is increased, the mobility of elliptic and circular disks develops a quite differ-
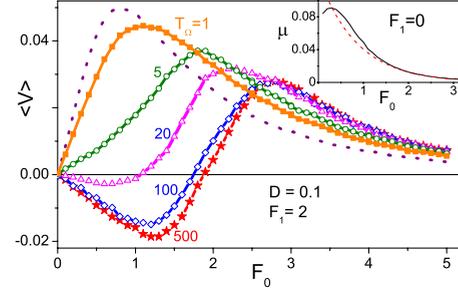
FIG. 2. (Color online) ANM for a driven-pulsated elongated Brownian particle: current $\langle v \rangle$ vs static bias F_0 in the presence of square-wave drives with amplitude $F_1 = 2$ and different periods T_Ω (see legend). Other simulation parameters: Diffusion strengths $D = D_r = D_\phi = 0.1$; shape parameters $a = 0.05$, $b = 0.3$; compartment parameters $x_L = y_L = 1$, and $\Delta = 0.1$. Each data point for $\langle v \rangle \equiv \lim_{t \to \infty} \langle x(t) - x(0) \rangle / t$ was computed from a single trajectory with $t = 10^6$ and time-step 10^{-5}; the statistical error was estimated to be 5%, i.e., of the order of the symbol size. Note, for a comparison, that the compartment traversal time is $\tau_0 = 7$ and the diffusive relaxation times are $\tau_D^{(x)} = \tau_D^{(y)} = 5$. The dotted curve represents $v(F)$ at zero ac-drive, $F_1 = 0$. Inset: the corresponding mobility curve (solid curve), $\mu(F)$, is compared with the analytical estimate of Eq. (4) (dashed curve) for $F_m = 0.86$.

ent F dependence. The mobility of a circular disk with $a = b < \Delta$, $\mu(F)$, is a concave function of F/D, which decays from $\mu_0 \equiv \mu(0)$ to $\mu_\infty \equiv \mu(F \to \infty) = (\Delta - a)/(y_L - a)$, with a power law slower than F^{-1} [18]. In the case of an elliptic disk with $a < \Delta < b$, reaching the escape angle ϕ^* can be regarded as a noise activated process with energy barrier proportional to F. Pore crossing will then be controlled mostly by the *rotational* fluctuations, with approximate escape time

$$\tau_0(F) = \tau_0 \exp(F/F_m), \quad (2)$$

where $F_m = 2D/(b \cos \phi^* - a)$ is the total activation force, the factor 2 accounts for the two directions of rotation, and τ_0 is the compartment traversal time, x_L/F, divided by the probability, $p = (\Delta - a)/(y_L - a)$, that the disk slides through the pore without an additional rotation. The reciprocal of τ_0 plays the role of an effective attack frequency. This estimate for the particle crossing time surely holds good for $b \gg \Delta$ and $F \gg F_m$, where

$$\tau_0 \ll \tau_D^{(x)}, \tau_D^{(y)} \ll \tau_0(F), \quad (3)$$

with $\tau_D^{(x)} = x_L^2/2D$ and $\tau_D^{(y)} = y_L^2/2D$ denoting, respectively, the longitudinal and transverse relaxation times.

The curve $\mu(F)$ for an elongated particle is thus concave for $F < D/x_L$ [18] and decays exponentially for $F \gg F_m$, like

$$\mu(F) \simeq \frac{x_L}{F\tau_0(F)} = 2p \exp(-F/F_m), \quad (4)$$

see inset in Fig. 2. Correspondingly, $v(F)$ increases like $\mu_0 F$ at small F and decays to zero like $x_L/\tau(F)$ at large F, going through a maximum for $F \sim F_m$, as confirmed by our simulations, see Fig. 2.

A convincing evidence for ANM has been obtained by simultaneously applying to the elliptic disk a tunable dc force, F_0, and a low-frequency, square-wave ac force, $F_{ac}(t)$, with amplitude $F_1 > F_0 \geq 0$. The characteristics curves $\langle v \rangle$ vs F_0 plotted in Fig. 2 exhibit a negative ANM branch only for sufficiently long ac-drive periods and $F_0 < F_1$; for $F_0 > F_1$, however, the current is always oriented in the F_0 direction, no matter what T_Ω.

This behavior can be explained in the *adiabatic* regime, where a half drive period, $T_\Omega/2$, is larger than all the drift and diffusion times inside a channel compartment, namely, τ_0, $\tau_D^{(x)}$, and $\tau_D^{(y)}$ [19]. Note that in the opposite regime, ANM is suppressed. The net current can then be approximated by

$$\langle v(F_0) \rangle = \frac{1}{2}[v(F_1 + F_0) - v(F_1 - F_0)]. \quad (5)$$

As the curve $v(F)$ peaks at $F \sim F_m$, we expect $\langle v(F_0) \rangle$ to develop a negative minimum for $F_0 = F_1 - F_m$ and a positive maximum for $F_0 = F_1 + F_m$, as shown in Fig. 2. As this holds true only for $F_1 > F_m$, the two peaks have upper bounds

$$|\langle v(F_1 - F_m) \rangle| \lesssim \langle v(F_1 + F_m) \rangle \lesssim v(F_m). \quad (6)$$

For a more quantitative analysis of this phenomenon, we rewrite $v(F_1 \pm F_0) = (F_1 \pm F_0)\mu(F_1 \pm F_0)$, so that the ANM condition, $\langle v \rangle < 0$, reads

$$\frac{F_1 - F_0}{F_1 + F_0} > \frac{\mu(F_1 + F_0)}{\mu(F_1 - F_0)} \simeq e^{-2F_0/F_m}. \quad (7)$$

The approximate equality on the rhs applies for $0 < F_0 < F_1 - F_m$, where

$$\mu(F_1 \pm F_0) \simeq \mu(F_1)e^{\mp F_0/F_m}. \quad (8)$$

The above inequality is satisfied for $0 < F_0 < F^*$, with the turning point, F^*, shifting toward zero in the limit $F_1 \to F_m+$, and toward F_1 in the opposite limit, $F_1 \gg F_m$. The approximate equality in Eq. (7) leads to slightly overestimating F^*, with no prejudice of our conclusion: In the adiabatic regime, ANM occurs in an appropriate F_0 interval $(0, F^*)$ only provided that $F_1 > F_m$.

Finally, we notice that for $F_0 > F_1 > F_m$ the net current reads

$$\langle v(F_0) \rangle = \frac{1}{2}[v(F_0 + F_1) + v(F_0 - F_1)] \quad (9)$$

and for extremely large F_0, it decays to zero like $\langle v(F_0) \rangle \sim \frac{1}{2}v(F_0 - F_1)$. Correspondingly, our simulation data in the neighborhood of the turning point $F^* \sim F_1$ are reasonably well reproduced by the linear fitting law, $\langle v(F_0) \rangle \sim (\mu_0/2)(F_1 - F_0)$.

IV. SELECTIVITY AND OPTIMIZATION CRITERIA

In view of future experimental implementations of the proposed ANM mechanism, we now analyze in detail its sensitivity with respect to both the drive and the particle parameters.

We start noticing that the most prominent ANM effect is produced, in fact, by the square waveform $F_{ac}(t)$ adopted in
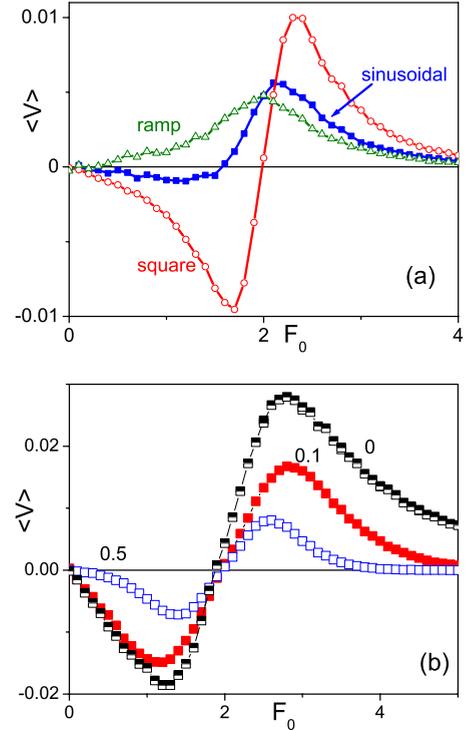
FIG. 3. (Color online) (a) Drive waveform dependence: $\langle v \rangle$ vs F_0 for three waveforms of $F_{ac}(t)$, square (as in Fig. 2), sinusoidal and ramped, all with $F_1=2$, $D=0.02$, and $T_\Omega=10^3$. (b) Particle inertia dependence: $\langle v \rangle$ vs F_0 for three values of $m=I$, see text. Other simulation parameters are $F_1=2$, $D=0.1$, and $T_\Omega=500$.

Fig. 2. For the sake of a comparison, in Fig. 3(a), we plotted $\langle v(F_0) \rangle$ also for other, inversion-symmetric waveforms $F_{ac}(t)$ with the same amplitude and period, in particular, sinusoidal and up-down ramped waveforms. For a ramped ac drive, no ANM can occur, because in the adiabatic regime

$$\langle v(F_0) \rangle = \frac{1}{2F_1}\int_{F_1-F_0}^{F_1+F_0} v(F)dF \geq 0. \quad (10)$$

For a sinusoidal ac drive, the ANM effect can be shown analytically to diminish in magnitude and shrink to a narrower interval $(0, F^*)$ than obtained for the corresponding square waveform. The latter is thus the optimal ac-drive waveform to operate an ANM device.

To quantify the robustness of this effect against the damping conditions, inertia was added to the model by replacing the lhs in the Langevin Eqs. (1) as follows:

$$\frac{d\vec{r}}{dt} \to \frac{d\vec{r}}{dt} - m\frac{d^2\vec{r}}{dt^2}, \quad (11a)$$

$$\frac{d\phi}{dt} \to \frac{d\phi}{dt} - I\frac{d^2\phi}{d^2t}. \quad (11b)$$

In Fig. 3(b), we compare ANM characteristics curves for growing values of the (rescaled) particle mass, m, and moment of inertia, I: ANM is gradually suppressed by increasing inertia. This is no serious limitation, as in most experi-
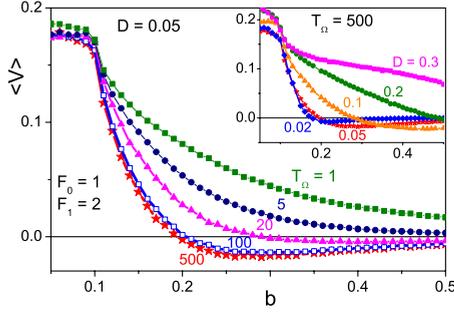
FIG. 4. (Color online) Particle elongation dependence: $\langle v \rangle$ vs b for different values of T_Ω (main panel) and of D (inset). Other simulation parameters: square-wave ac-drive with amplitude strength $F_1 = 2$, and bias $F_0 = 1$, $a = 0.05$, $x_L = y_L = 1$, and $\Delta = 0.1$.

ments rectifiers operate, indeed, under overdamped, or zero mass, conditions [8].

We analyze next how selective the ANM effect is versus the geometric and diffusive properties of the transported particles. In Fig. 4, we displayed the dependence of the net current on the particle elongation. One notices immediately that, when plotted versus b at constant values of the drive parameters, $\langle v \rangle$ starts out positive and then turns negative for b larger than a certain threshold, b^*, which appears to increase with either raising D (figure inset) or lowering T_Ω (main panel).

Our adiabatic argument provides a simple explanation for these findings, as well. We recall that the mobility curve $\mu(F)$ decays exponentially on a scale $F_m \propto b^{-1}$. As a consequence, for $b \to \infty$, Eq. (5) boils down to $\langle v \rangle \simeq -\frac{1}{2} v(F_1 - F_0)$, which means that $\langle v \rangle$ tends to zero from negative values, in agreement with our data. For $b \lesssim \Delta$ the particle flows through the pores, no matter what the orientation, ϕ, of its major axis. Therefore, $\langle v \rangle$ becomes insensitive to the particle elongation (main panel), while retaining its known D dependence (inset).

The actual value of b^* is determined by the general ANM condition (7). On making use of the approximation on the rhs of that equation, one easily proves the existence of the threshold b^* for any geometry and drive parameter set. We caution that this way one may underestimate b^* and, therefore, the predicted dependence $b^* \propto D$ holds qualitatively, only (see inset of Fig. 4). Of course, when D is raised so that b^* grows larger than the spatial dimensions of a channel compartment, then ANM is suppressed altogether.

The dependence of the current on the fluctuation intensities is illustrated in Fig. 5. We consider first the case $D_r = D_\phi = D$ (figure inset). The dependence of $\langle v \rangle$ on D can be analyzed following the approach introduced to interpret the results in Fig. 4. On recalling that $F_m \propto D$, in the limit $D \to \infty$, the ac-drive amplitude ends up being smaller than F_m, $F_m > F_1$, thus suppressing ANM. In the opposite limit, $D \to 0$, F_m vanishes and ANM is predicted to occur for any dc drive such that $0 < F_0 < F_1$. Indeed, from Eq. (5) we obtain $\mu(F_1 \pm F_0) \to \mu_0$ or $\langle v \rangle \to \mu_0 F_0 > 0$, for $D \to \infty$ (marked in figure by horizontal arrows), and $\langle v \rangle \simeq -\frac{1}{2} v(F_1 - F_0) \to 0-$, for $D \to 0$. On using D as a control parameter, ANM is thus restricted to low noise, $0 < D < D^*$, with the threshold D^* also obtainable from the ANM condition (7).
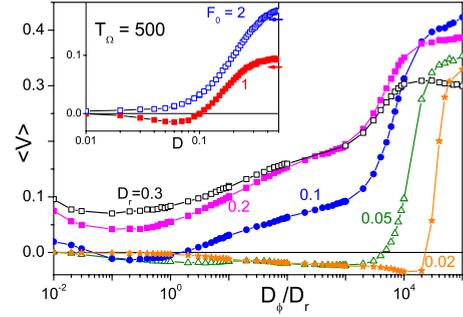
FIG. 5. (Color online) Rotational translational diffusion dependence: $\langle v \rangle$ vs D_ϕ / D_r for different values of D_r (see legend). Inset: $\langle v \rangle$ vs $D = D_r = D_\phi$ with $D_\phi / D_r = 1$. The arrows mark the asymptotes predicted in the text. Other simulation parameters are as in Fig. 4 with $b = 0.3$.

We consider next the more general case when D_r and D_ϕ can be independently varied, while keeping a and b fixed. In Fig. 5, $\langle v \rangle$ has been plotted versus D_ϕ / D_r for different values of D_r. The two opposite limits of the net current, $\langle v \rangle_0$, for $D_\phi / D_r \to 0$, and $\langle v \rangle_\infty$, for $D_\phi / D_r \to \infty$, are both positive with $\langle v \rangle_0 < \langle v \rangle_\infty$. In between, the magnitude of the ANM effect is seemingly not much sensitive to D_ϕ / D_r over several orders of magnitude, which allows us to generalize the conclusions drawn above for $D_\phi / D_r = 1$ to the case of realistic extended particles. Note that $\langle v \rangle_0$ is non-null because an elliptic disk with $a < \Delta < b$ can diffuse across a pore even in the limit $D_\phi \to 0$, where the adiabatic argument fails, thanks to the sole translational fluctuations. In view of the crossing condition $|\phi| < \phi^*$, an elongated particle can be handled as a circular one with radius smaller that Δ, see Fig. 4, but crossing probability $2\phi^*/\pi$. This argument can be extended to the case of $\langle v \rangle_\infty$, with the important difference that for $D_\phi \to \infty$ the particle has crossing probability one. Both $\langle v \rangle_0$ and $\langle v \rangle_\infty$ are thus positive, with $\langle v \rangle_0$ relatively smaller than $\langle v \rangle_\infty$.

V. CONCLUDING REMARKS

The ANM model presented in this work, although stylized, lends itself to interesting nanotechnological applications [8,19]. A typical reference case is represented by the transport of hydrated DNA fragments across narrow compartmentalized channels [20]. Rodlike DNA fragments 30–40 nm in length and 1–2 nm in (hydrated) diameter are easily accessible [21]; their elongation ratio is about three times larger than b/a in Fig. 2, but still within the ANM range of Fig. 4. Artificial nanopores can be transmission-electron-microscope (TEM)-drilled in 10 nm thin SiO$_2$ membranes with reproducible diameters of 5 nm, or less [20], which is consistent with the elongation selectivity condition $a < \Delta < b$ assumed throughout this work. Moreover, the measured D_ϕ / D_r ratio for the hydrated DNA fragments of Ref. [21] falls in the range 100–200, in dimensionless units, where ANM can also occur, as shown in Fig. 5, for an appropriate choice of the drive parameters. To this regard, we remind that experiments on DNA translocation across artificial nanopores require applied electrical fields of the order of 10–100 kV/cm [22]; if applied to the DNA rods of Ref. [21],

electrical fields of that intensity, or less, would satisfy the ANM condition of Eq. (7) with $F_1 > F_m$ at room temperature.

The ANM characteristics curves plotted in Figs. 2 and 5, being quite selective with respect to the particle shape, suggest the possibility of developing artificial devices that efficiently operate as *geometric sieves* for nanoparticles. Our model was stylized to capture the key mechanism responsible for the occurrence of ANM in symmetric channels. The mechanism summarized by Eqs. (2) and (7), however, clearly does not depend on the dimensionality of the channel (experiments can then be carried out in 3D geometries), but can be impacted by other competing effects: (i) Pore selectivity. For a given translocating molecule, the actual crossing time varies with the wall structure inside the pore and in the vicinity of its opening [23]; (ii) Electrophoretic effects. The inhomogeneous electrical field generated by the electrolyte flow across the pores acts on the orientation of drifting spheroidal particles [24]. System specific effects (i) and (ii) can readily be incorporated in our model by adding appropriate potential terms, $U_r(x,y)$ and $U_\phi(\phi)$, to the Langevin Eqs. (1).

[1] P. Reimann, R. Kawai, C. Van den Broeck, and P. Hänggi, Europhys. Lett. **45**, 545 (1999).

[2] B. Cleuren and C. Van den Broeck, EPL **54**, 1 (2001).

[3] R. Eichhorn, P. Reimann, and P. Hänggi, Phys. Rev. Lett. **88**, 190601 (2002).

[4] R. Eichhorn, P. Reimann, and P. Hänggi, Phys. Rev. E **66**, 066132 (2002).

[5] B. I. Sturman and V. M. Fridkin, *The Photovoltaic and Photorefractive Effects in Noncentrosymmetric Materials* (Gordon and Breach Science Publishers, Philadelphia, 1992).

[6] R. A. Höpfel, J. Shah, P. A. Wolff, and A. C. Gossard, Phys. Rev. Lett. **56**, 2736 (1986).

[7] B. J. Keay, S. Zeuner, S. J. Allen, K. D. Maranowski, A. C. Gossard, U. Bhattacharya, and M. J. W. Rodwell, Phys. Rev. Lett. **75**, 4102 (1995).

[8] P. Hänggi and F. Marchesoni, Rev. Mod. Phys. **81**, 387 (2009).

[9] L. Machura, M. Kostur, P. Talkner, J. Luczka, and P. Hänggi, Phys. Rev. Lett. **98**, 040601 (2007).

[10] M. Kostur, L. Machura, P. Talkner, P. Hänggi, and J. Luczka, Phys. Rev. B **77**, 104509 (2008).

[11] D. Speer, R. Eichhorn, and P. Reimann, Phys. Rev. E **76**, 051110 (2007).

[12] A. Ros, R. Eichhorn, J. Regtmeier, T. T. Duong, P. Reimann, and D. Anselmetti, Nature (London) **436**, 928 (2005).

[13] J. Nagel, D. Speer, T. Gaber, A. Sterck, R. Eichhorn, P. Reimann, K. Ilin, M. Siegel, D. Koelle, and R. Kleiner, Phys. Rev. Lett. **100**, 217001 (2008).

[14] B. Hille, *Ion Channels of Excitable Membranes* (Sinauer, Sunderland, 2001).

[15] J. Kärger and D. M. Ruthven, *Diffusion in Zeolites and other Microporous Solids* (Wiley, New York, 1992).

[16] M. Borromeo and F. Marchesoni, Chem. Phys. **375**, 536 (2010).

[17] P. Hänggi, R. Bartussek, P. Talkner, and J. Łuczka, Europhys. Lett. **35**, 315 (1996).

[18] F. Marchesoni and S. Savel'ev, Phys. Rev. E **80**, 011120 (2009).

[19] P. S. Burada, P. Hänggi, F. Marchesoni, G. Schmid, and P. Talkner, ChemPhysChem **10**, 45 (2009).

[20] C. Dekker, Nat. Nanotechnol. **2**, 209 (2007).

[21] M. M. Tirado, C. L. Martínez, and J. G. de la Torre, J. Chem. Phys. **81**, 2047 (1984).

[22] For a review see: K. Healy, Nanomedicine **2**, 459 (2007).

[23] S. M. Iqbal, D. Akin, and R. Bashir, Nat. Nanotechnol. **2**, 243 (2007).

[24] Y. Solomentsev and J. L. Anderson, Ind. Eng. Chem. Res. **34**, 3231 (1995).